Electronic Supplementary Information (ESI)

Controlling the Thermal Switching in Upconverting Nanoparticles Through Surface Chemistry

Eduardo D. Martínez[a,*], Alí F. García-Flores[b], Albano N. Carneiro Neto[c], Carlos D. S. Brites[c], Luís D. Carlos[c], Ricardo R. Urbano[b], Carlos Rettori[b,d]

a. Instituto de Nanociencia y Nanotecnología (INN), Centro Atómico Bariloche, Comisión Nacional de Energía Atómica (CNEA), Consejo Nacional de Investigaciones Científicas y Técnicas (CONICET), Av. E. Bustillo 9500, R8402AGP, S. C. de Bariloche, Río Negro, Argentina.

b. "Gleb Wataghin" Institute of Physics (IFGW), University of Campinas (UNICAMP), 13083-859, Campinas, SP, Brazil.

c. Phantom-g, CICECO-Aveiro Institute of Materials, Physics Department, University of Aveiro, 3810-193 Aveiro, Portugal.

d. CCNH, Federal University of ABC (UFABC), 09210-580, Santo André, SP, Brazil.

1. Chemicals

Polyvinylpirrolidone (PVP) average mol. wt. 10000, poly(acrylic acid, sodium salt) (PAA) Mw<15000, $Na(COOCF_3)$, oleic acid (OA) technical grade, 90% and 1-octadecene (ODE) technical grade, 90% were purchased from Sigma-Aldrich Co. and used without further purification. $Gd(COOCH_3)_3$ hydrate 99.9% was purchased from Alfa Aesar. Rare-earth acetates were prepared in our laboratory from the corresponding rare-earth oxides (X_2O_3, X=Y, Yb, Tm and Er) purchased from Sigma-Aldrich. For this, 1-2 g of each oxide were added in a 500 mL round flask containing 30–50 mL of a 50 % solution of acetic (CH_3COOH) acid. The mixture was refluxed until the complete dissolution of the oxides leading to a clear solution, which took 1-2 hours. The solution was then moved to a Pyrex open vessel and maintained at 60 °C to evaporate the acid solution. The acetates salts precipitated and the dry powder was extracted.

2. Synthesis of core UCNPs β-$NaYF_4$:Yb, Er

Small-sized β-$NaYF_4$ UCNPs (~20 nm) were synthesized by the co-precipitation route using rare-earth acetates as the main precursors.[1] Stock solutions of $X(COOCH_3)_3$ (X= Y, Yb, and Er) 0.2M in water were prepared. A total of 4.65 mL $Y(COOCH_3)_3$ stock solution (corresponding to 0.93 mmol), 0.25 mL of $Yb(COOCH_3)_3$ (0.05 mmol) and 0.01 mL of $Er(COOCH_3)_3$ (0.002 mmol) was added to a 200 mL round flask containing ODE (15 mL) and OA (6 mL). The mixture was heated up to 130 °C for 60 minutes to evaporate the water and then cooled down to room temperature. At this point, a freshly prepared mixture of a solution of NaOH in methanol (2.5 mL, 1M) and a solution of NH_4F in methanol (10.1 mL, 0.4 M) was rapidly injected. The flask was heated to 50 °C for 30 minutes and then it was sealed and connected to a vacuum line. The temperature was

raised to 100 °C and maintained for 15 minutes. The vacuum pump was turned off and argon flux was injected. A reflux system was mounted, and the temperature was increased to 310 °C. After a total reaction time of 90 minutes the flask was removed from the mantle. Extraction of the UCNPs was performed by adding excess anhydrous ethanol and centrifugation using 15 mL Falcon tubes. In each tube, the UCNPs were redispersed in 4 mL of cyclohexane, and ethanol was added to complete the volume. The procedure was repeated two times but adding 4 mL of methanol as well. After extraction through repeated cycles of centrifugation and washing with anhydrous ethanol, core nanoparticles were dispersed in cyclohexane at a concentration of ~37 $g \cdot L^{-1}$.

3. Synthesis of core-shell β-$NaYF_4$:Yb,Er@$NaGdF_4$:Yb:Tm

A layer-by-layer method was used for the synthesis of a $NaGd_{0.6950}Yb_{0.30}Tm_{0.005}F_4$ shell.[2] A 1 M stock solution of Gd, Yb and Tm acetates with the appropriate molar fractions in OA was first prepared by adding the precursors to OA and heating above 120 °C under argon flux. Same procedure was applied to prepare a 0.4 M solution of $Na(COOCF_3)$ in OA. A shell layer was grown by adding 4.5 mL of the core-UCNPs colloid in cyclohexane into a three neck 200 mL round flask containing OA (4 mL) and ODE (6 mL). The temperature was raised up to 80 °C under vacuum to evaporate the cyclohexane. Then, argon flux was connected, and the temperature was raised up to 280 °C. At this point, a first injection of 2 mL of the RE-OA stock solution was injected dropwise. After 15 minutes, 1 mL of the $Na(COOCF_3)$-OA solution was added in the same manner. After 15 minutes, the process was repeated. Three cycles of injection of each reactant were performed in total. After completing the reaction the flask was removed from the mantle. Core@shell UCNPs were extracted by repeated cycles of centrifugation after washing in anhydrous ethanol and finally dispersed in cyclohexane.

4. Surface modification

Surface modification of core UCNPs was performed following protocols reported by Bogdan et al.[3] and generalized by Kong et al.[4] Here, 1 ml of the core-UCNPs colloid in cyclohexane was added to 2 mL of an HCl 0.1M solution in ethanol in a 8 mL glass test tube. The tube was sealed and place in an ultrasonic bath for at least 40 minutes. The UCNPs, supposedly free of the OA capping, were extracted by centrifugation at 4000 rpm for 15 minutes. Two cycles of washing in ethanol and centrifugation followed. Then, the extracted UCNPs were dispersed in 1 mL of water. A small aliquot of this colloid was separated constituting the uncapped-UCNPs sample. Aqueous solutions of the polymers PAA and PVP (50 mg in 9 mL) were prepared and the pH was adjusted to 8 through dropwise addition of a solution of NaOH. Under strong agitation, 0.5 mL

of the UCNPs in water was slowly added to the solutions of each polymer and remain for 2 h under stirring. 10 mL of diethyleneglycol (DEG) were then added and heated above 100 °C to evaporate the water. After complete evaporation of water, the UCNPs and polymers in DEG were poured into seal flasks and heated in an oven at 115 °C for at least 2 h. Finally, the polymer coated UCNPs were extracted by repeated cycles of washing and centrifugation in water:ethanol mixtures until a final dispersion in water is prepared.

5. Thermometric characterization of the luminescent thermometer

The relative thermal sensitivity of the particles is calculated using:

$$S_r = \frac{1}{\Delta}\left|\frac{\partial \Delta}{\partial T}\right| = \frac{\delta E}{k_B T^2} \quad \text{(S1)}$$

where δE is the separation between the thermally coupled energetic levels, k_B is the Boltzmann constant, T the absolute temperature and Δ the thermometric parameter defined by Equation 1 of the manuscript. The uncertainty of the thermometer is:

$$\delta T = \frac{1}{S_r}\frac{\delta \Delta}{\Delta} \quad \text{(S2)}$$

where $\delta\Delta/\Delta$ is the relative error in the thermometric parameter (experimentally determined to be $\delta\Delta/\Delta$ = 0.1 %).

The thermometer's repeatability upon temperature cycling is quantified using:

$$R = 1 - \frac{max(|\Delta_i - \Delta_c|)}{\Delta_c} \quad \text{(S3)}$$

where Δ_c is the mean thermometric parameter and Δ_i its value for each measurement.

The error in the estimation of the temperature using Equation 1 of the manuscript is given by:

$$\Delta T = \frac{1}{T^2}\sqrt{\left(\frac{\Delta T_0}{T_0}\right)^2 + \left(\frac{k_B \times \Delta(\delta E)}{\delta E^2}\right)^2 + \left(\frac{k_B}{\delta E}\frac{\delta \Delta}{\Delta}\right)^2 + \left(\frac{k_B}{\delta E \times \Delta}\frac{\delta \Delta_0}{\Delta_0}\right)^2} \quad \text{(S4)}$$

where ΔT_0=0.1 K is the uncertainty in T_0, and $\Delta(\delta E)$ is the uncertainty in the determination of δE.[5–7]

Electronic Supplementary Information (ESI)

6 Experimental Set-Up

Real-time acquisition of UCL during the thermal cycling was realized on a homemade experimental set-up, a scheme of which is depicted in Figure S1. An aliquot of the UCNPs colloid in cyclohexane was deposited on a piece of a silicon wafer and left for the solvent to evaporate completely. The piece was mounted on a Peltier plate (60W, Tec1 12706) using a high thermal conductivity paste for optimal thermal contact. A type K thermocouple was also contacted to the heating plate with the thermal paste a few millimeters aside from the sample. The power supply of the heating element was automatically turned on and off through an Arduino controlled 5V relay. At an oblique angle, a CW collimated 976 nm laser beam (BL976-PAG900 FBG stabilized laser, ThorLabs, inc.) with a nominal power of 300 mW impinged on the sample producing a spot of about 1 mm^2 in size (power density: ~30 $W{\cdot}cm^2$). The emissions from UCL were collected by a collecting lens with 50 mm focus length aligned with an optical fiber head inside a ad-hoc made mounting casing. A NIR short pass filter was included to cut-off the excitation laser. Emission spectra were registered continuously through a QEPro spectrometer (Ocean Optics) using integration times of 5 s to 15 s depending on the emission intensity. Near the measuring stage, a DHT11 sensor was used to measure the relative humidity in the environment, which was stable within 45% to 55% during all measurements.

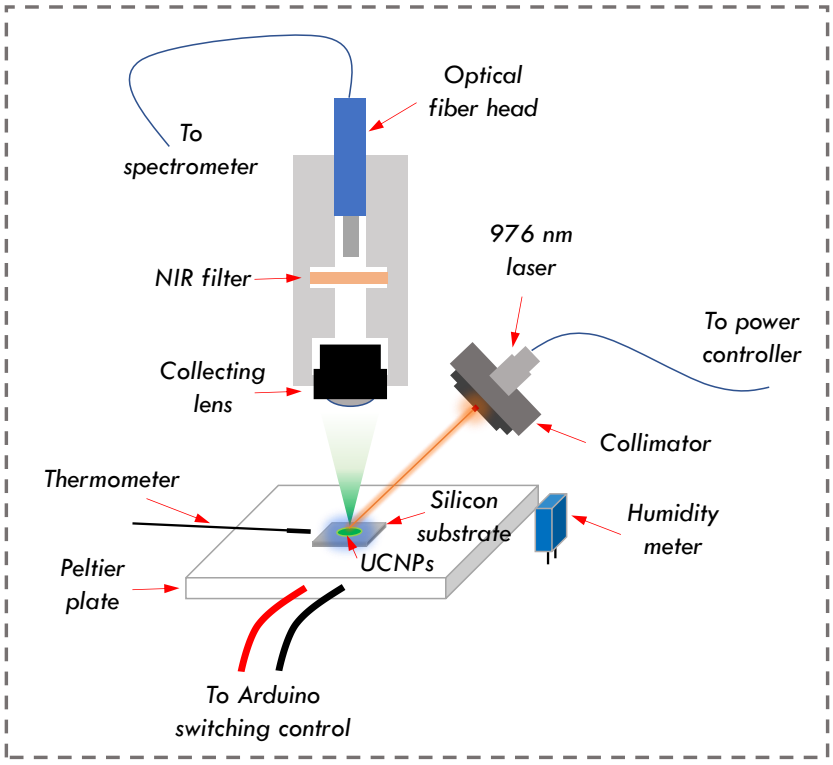

Figure S1 Experimental set-up used for the real-time measurement of UCL during thermal cycling.

Electronic Supplementary Information (ESI)

7 Additional measurements

7.1 Tm^{3+} emissions from core-shell-UCNPs

The complete emission spectra of the core-shell UCNPs containing Yb^{3+}(5%)-Er^{3+}(2%) in the core and Yb^{3+}(30%)-Tm^{3+}(0.5%) in the shell are presented in Figure S2a. Clearly, the emission intensity of the Er^{3+} ions is higher than that of Tm^{3+} ions regardless the lower content of Yb^{3+} (sensitizer) in the core region. For Tm^{3+}, only the emissions at ~800 nm (Figure S2b), corresponding to the $^3H_4 \rightarrow {}^3H_6$ transition, were intense enough for a confident analysis. From the integration of the emission peak, it is clear in Figure S2c that the thermal dependence of the emissions of Tm^{3+} ions located in the shell shows a thermal enhancement behaviour, following the same trend as that of Er^{3+} in UCNPs without a shell, as presented in Figure 3 in the main text. Interestingly, the overshoot phenomena also occurred here immediately after turning the heating source off. The integrated intensity I_{NIR} as a function of the thermometric parameter Δ is shown in Figure 2Sd displaying the characteristic hysteresis loop for the thermal enhancement mediated by the water adsorption/desorption mechanism.

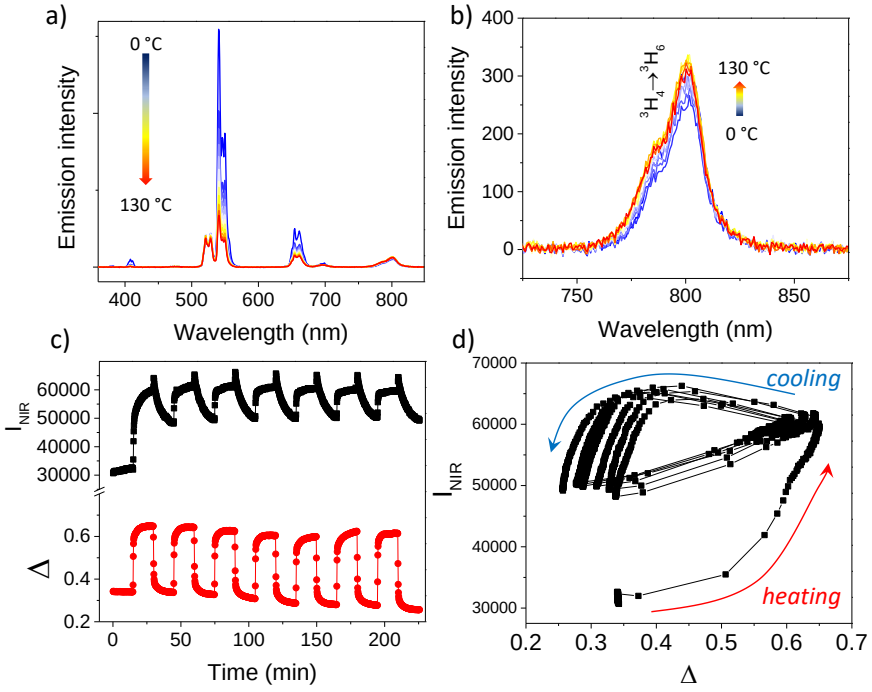

Figure S2 a) Extended emission spectra of UCNPs-Core-shell. b) Emission line at 800 nm corresponding to the transition $^3H_4 \rightarrow {}^3H_6$ of Tm^{3+} (I_{NIR}) in the shell layer. Integrated intensity of the I_{NIR} emissions upon thermal cycling as a function of c) time and d) the thermometric parameter.

7.2 Small-size Er^{3+}-doped UCNPs

We measured the UCL under thermal cycling on UCNPs of smaller size and with a different composition to those discussed in the main text. Here, β-$NaGd_xF_4$:Yb20%:Er2% (x=0.78) were synthesized though the co-precipitation method described above, resulting in OA-capped UCNPs with a mean size of (8.0 ± 2.5) nm. As shown in Figure S3a, these particles show a similar thermal enhancement behavior to the UCNPs-OA presented in the main text. However, the emission intensity is lower due to their reduced size. In order to increase the quantum yield for UCL, a shell layer of $NaGd_{0.8}F_4$:Yb20% was grown resulting in core-shell UCNPs with a mean size of (10.5±1.5) nm, meaning a thin shell thickness of ~1.25 nm. For these particles, a similar thermal enhancement effect was observed together with the overshoot peak after turning the heating source off. Again, the overshoot was more clearly appreciated for the $^4S_{3/2} \rightarrow {}^4I_{15/2}$ transition.

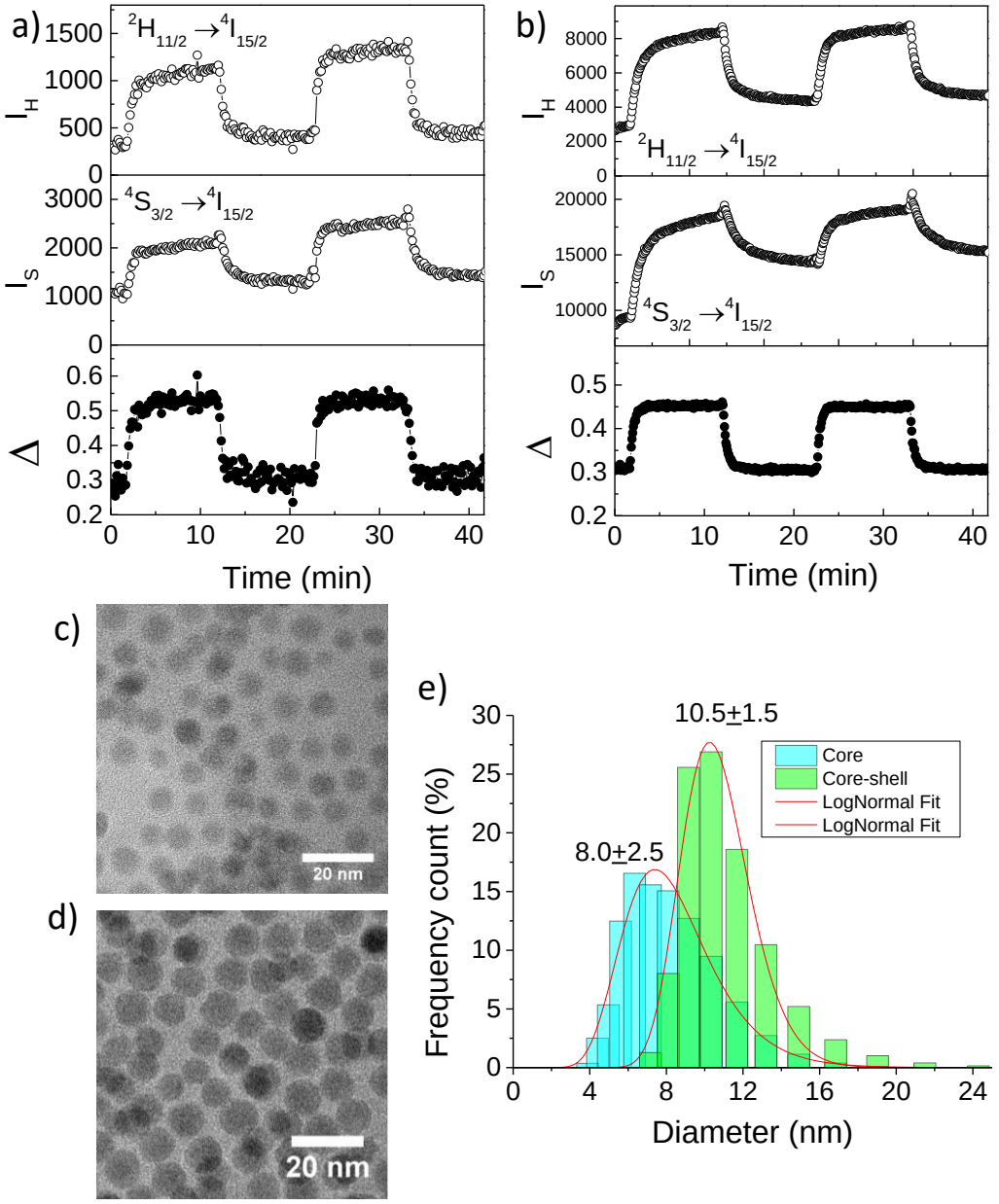

Figure S3 Thermal cycling and the overshoot phenomenon in small-size UCNPs β-$NaGd_{0.78}F_4$:Yb20%:Er2% a) without and b) with shell of $NaGd_{0.8}F_4$:Yb20%. TEM images of c) core and d) core-shell UCNPs. d) Particle size distribution of core and core-shell UCNPs.

8 Modelling the surface defect states (SDS)

8.1 Energy transfer from the surface defect state to Er^{3+} ion

To estimate the non-radiative energy transfer rates from the surface defects states (SDS) to Er^{3+} ions, it is essential to consider the following premises:

i) SDS can act as donor (D) states and its energetic position is sensitive to the coating material

ii) These states are loaded from the ground state population of the material when the heating source is on

iii) SDS has vibronic states that are thermally populated and decay fast to the lower vibronic state when the heating source is turned off.

Considering the above premises, the non-radiative energy transfer rates can be calculated taking into account the dipole-dipole (W_{d-d}), dipole–multipole (W_{d-m}), and exchange (W_{ex}) mechanisms [8–12] according to Eqs. (S5)–(S7).

For the dipole–multipole (2^K–poles, $K = 2, 4$, and 6, respectively) contribution:

$$W_{d-m} = \frac{S_L}{(2J+1)G}\frac{2\pi e^2}{\hbar}\sum_K (K+1)\frac{\langle r^K\rangle^2}{(R_L^{K+2})^2}\langle f\|C^{(K)}\|f\rangle^2(1-\sigma_K)^2 \times \langle \psi^* J^*\|U^{(K)}\|\psi J\rangle^2 F \quad \text{(S5)}$$

where S_L is the dipole strength of the D state, $\langle r^K\rangle$ are the 4*f* radial integrals [13], G is the D state degeneracy (it will be considered that the defect state is a singlet, $G = 1$), R_L is the donor–acceptor states distance (4 Å is a considerably acceptable value), $\langle \|C^{(K)}\| \rangle$ is the reduced matrix element of Racah's tensor operator, $(1-\sigma_K)$ are the 4*f* shielding factor [13], and $\langle \|U^{(K)}\| \rangle$ are the reduced matrix elements and their values are tabulated in Ref. [14].

For the dipole-dipole contribution:

$$W_{d-d} = \frac{S_L(1-\sigma_1)^2}{(2J+1)G}\frac{4\pi}{\hbar}\frac{e^2}{R_L^6}\sum_\lambda \Omega_K^{FED}\langle \psi^* J^*\|U^{(K)}\|\psi J\rangle^2 F \quad \text{(S6)}$$

where the 4*f*-4*f* intensity parameters Ω_K^{FED} (K = 2, 4, and 6) were obtained by using only the forced electric dipole mechanism (FED) and it was employed the Simple Overlap Model [15,16] to calculate the Ω_K^{FED}.

For the exchange contribution:

$$W_{ex} = \frac{\langle 4f|D\rangle^4}{(2J+1)}\frac{8\pi}{3\hbar}\frac{e^2}{R_L^4}\langle \psi^* J^*\|S\|\psi J\rangle^2\sum_m \left|\langle\phi|\sum_j \mu_z(j)s_m(j)\,|\phi^*\rangle\right|^2 F \quad \text{(S7)}$$

where $\langle 4f|D\rangle$ is the overlap integral between the SDS and the 4*f* state (Er^{3+}) at R_L distance, s_m the spin operator of electron j in the donor, μ_z is the dipole operator (z-component), and $\langle \psi^* J^* \| S \| \psi J \rangle$ is the reduced matrix elements of the spin operator, which can be calculated using free-ion wavefunctions in the intermediate coupling scheme [12,17–19].

The spectral overlap factor (F in Eqs. (S5)-(S7)) considers the energy mismatch condition [9]. If the donor state is larger than the acceptor one (Ln^{3+} ions), F can be calculated as follows:

$$F = \frac{1}{\hbar\gamma_D}\sqrt{\frac{ln(2)}{\pi}}e^{-\left(\frac{\Delta}{\hbar\gamma_D}\right)^2 \ln(2)} \quad \text{(S8)}$$

where γ_D is the bandwidth at half-height of **D** state, it is considered the same order of magnitude as the electronic transitions governed by the spin selection rules ($\gamma_D \approx 3000\ cm^{-1}$). The Δ (in cm^{-1}) is the band maximum energy difference between **D** state and lanthanide ion **A** state, $\Delta = E_D - E_A$. Eq. (S8) must be multiplied by the barrier factor $\exp(\Delta/k_B T)$ when Δ is negative. The total energy transfer rate is given by:

$$W = W_{d-m} + W_{d-d} + W_{ex} \quad \text{(S9)}$$

More details on all quantities in the above equations can be found in Refs. [8–12,19–21].

One plausible question here is the possibility of interference between the two situations of the surface defects states in the energy transfer rates. However, Figure S4 disregard that because it shows that this effect could not happen between them once the influence of **Situation 1** is strong for the E_D far below the 16000 cm^{-1} while **Situation 2** comes strong for E_D close to 20000 cm^{-1}.

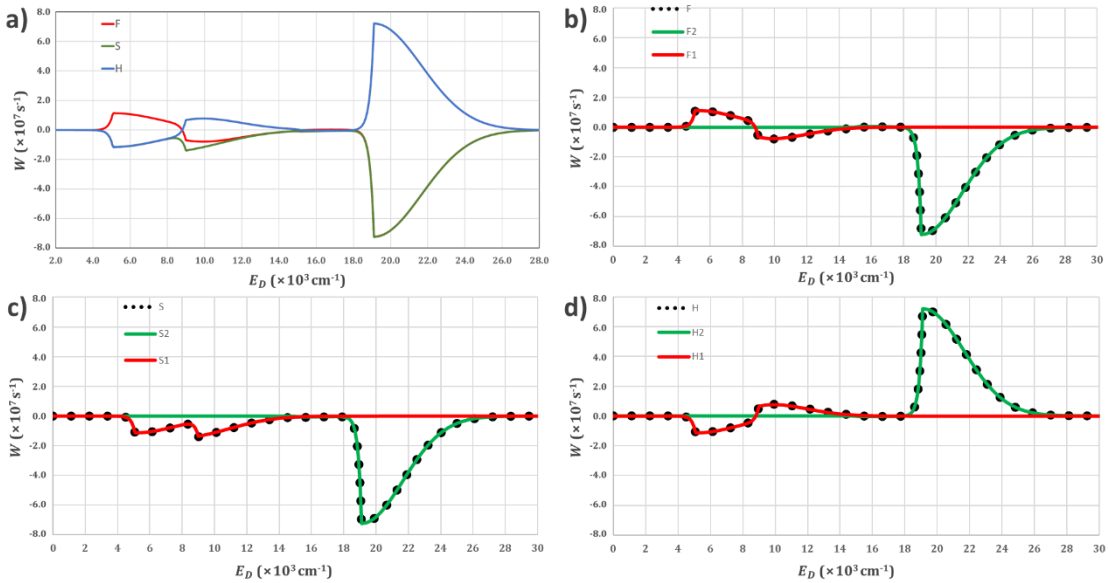

Figure S4. a) Differences between energy transfer rates from the SDS to Er^{3+} levels. Each line represents the difference between one and the others (*e.g.* S = $W\left({}^4S_{3/2}\right) - W\left({}^2H_{11/2}\right) - W\left({}^4F_{9/2}\right)$). The curves in **b)**, **c)**, and **d)** show that there are no significant overlapped rates between **Situations 1** (red lines) and **2** (green lines).

8.2 Multiphonon relaxation rates

The multiphonon decay rates between Er^{3+} levels (from $|N+1\rangle$ to $|N\rangle$ states) were calculated using the phenomenological energy gap law [14,22–25]:

$$W(0) = Be^{-\alpha \Delta E} \tag{S10}$$

where B and α are terms dependent on the host material and ΔE is the energy difference between $|N+1\rangle$ and $|N\rangle$ states. The multiphonon relaxation rate can be expressed with the temperature dependence $W(T)$ as follows:

$$W(T) = W(0)\left[1 - e^{-\left(\frac{\tilde{\omega}_{max}}{k_B T}\right)}\right]^{-\left(\frac{\Delta E}{\tilde{\omega}_{max}}\right)} \tag{S11}$$

where $\tilde{\omega}_{max}$ is the maximum phonon frequency and $k_B = 0.695035\ cm^{-1} \cdot K^{-1}$ is the Boltzmann constant. The curves in Figure S5, were obtained considering the energy levels differences in Ref. [14] and the empirical constants for the $LiYF_4$ crystal [25]: $\tilde{\omega}_{max} = 400\ cm^{-1}$, $B = 3.5 \times 10^7\ s^{-1}$, and $\alpha = 3.8 \times 10^{-3}$ cm.

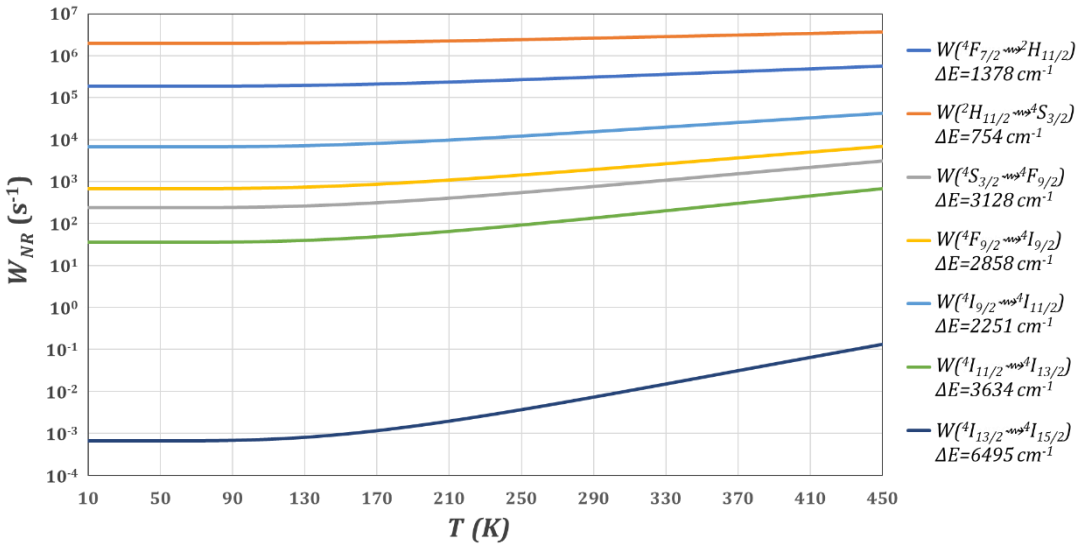

Figure S5. Multiphonon decay rates for the Er^{3+} ion (in $LiYF_4$ host material) calculated using the energy gap law (Eq. (S11)).

References

1 F. Wang, R. Deng and X. Liu, *Nat. Protoc.*, 2014, **9**, 1634–1644.

2 X. Li, D. Shen, J. Yang, C. Yao, R. Che, F. Zhang and D. Zhao, *Chem. Mater.*, 2013, **25**, 106–112.

3 N. Bogdan, F. Vetrone, G. A. Ozin and J. A. Capobianco, *Nano Lett.*, 2011, **11**, 835–840.

4 W. Kong, T. Sun, B. Chen, X. Chen, F. Ai, X. Zhu, M. Li, W. Zhang, G. Zhu and F. Wang, *Inorg. Chem.*, 2017, **56**, 872–877.

5 C. D. S. Brites, S. Balabhadra and L. D. Carlos, *Adv. Opt. Mater.*, 2019, **7**, 1801239.

6 C. D. S. Brites, A. Millán and L. D. Carlos, *Handb. Phys. Chem. Rare Earths*, 2016, **49**, 339–427.

7 C. D. S. Brites, P. P. Lima, N. J. O. Silva, A. Millán, V. S. Amaral, F. Palacio and L. D. Carlos, *Nanoscale*, 2012, **4**, 4799.

8 O. L. Malta, *J. Lumin.*, 1997, **71**, 229–236.

9 O. L. Malta and F. R. Gonçalves e Silva, *Spectrochim. Acta Part A Mol. Biomol. Spectrosc.*, 1998, **54**, 1593–1599.

10 R. Longo, F. R. Gonçalves e Silva and O. L. Malta, *Chem. Phys. Lett.*, 2000, **328**, 67–74.

11 O. L. Malta, *J. Non. Cryst. Solids*, 2008, **354**, 4770–4776.

12 A. N. Carneiro Neto, E. E. S. Teotonio, G. F. de Sá, H. F. Brito, J. Legendziewicz, L. D. Carlos, M. C. F. C. Felinto, P. Gawryszewska, R. T. Moura, R. L. Longo, W. M. Faustino and O. L. Malta, in *Handbook on the Physics and Chemistry of Rare Earths, volume 56*,

Elsevier, 2019, pp. 55–162.

13 S. Edvardsson and M. Klintenberg, *J. Alloys Compd.*, 1998, **275**–**277**, 230–233.

14 H. M. Carnall, W. T.; Crosswhite, H.; Crosswhite, *Energy level structure and transition probabilitiesof the trivalent lanthanides in LaF3*, Argonne, IL (United States), IL (United States), 1978.

15 O. L. Malta, *Chem. Phys. Lett.*, 1982, **88**, 353–356.

16 O. L. Malta, *Chem. Phys. Lett.*, 1982, **87**, 27–29.

17 G. S. Ofelt, *J. Chem. Phys.*, 1963, **38**, 2171–2180.

18 B. G. Wybourne, *Spectroscopic Properties of Rare Earths*, John Wiley & Sons, 1965.

19 E. Kasprzycka, A. N. Carneiro Neto, V. A. Trush, L. Jerzykiewicz, V. M. Amirkhanov, O. L. Malta, J. Legendziewicz and P. Gawryszewska, *J. Rare Earths*, 2020, **38**, 552–563.

20 F. R. G. e Silva and O. L. Malta, *J. Alloys Compd.*, 1997, **250**, 427–430.

21 H. F. Brito, O. M. L. Malta, M. C. F. C. Felinto and E. E. S. Teotonio, in *The chemistry of Metal Enolates*, ed. J. ZABICKY, Wiley-VCH Verlag GmbH, Weinheim, Germany, 2009, pp. 131–177.

22 R. Reisfeld and C. K. Jørgensen, *Lasers and Excited States of Rare Earths*, Springer-Verlag Berlin Heidelberg, 1st edn., 1977, vol. I.

23 H. W. Moos, *J. Lumin.*, 1970, **1**–**2**, 106–121.

24 B. Z. Malkin, in *Spectroscopic Properties of Rare Earths in Optical Materials. Springer Series in Materials Science, vol 83*, ed. J. B. Hull R., Parisi J., Osgood R.M., Warlimont H., Liu G., Springer, Berlin, Heidelberg, 2005, pp. 130–190.

25 L. A. Riseberg and M. J. Weber, in *Progress in Optics*, ed. E. Wolf, Elsevier, 1977, pp. 89–159.